RAA 2017 Vol. **17** No. **12**, 125(12pp) doi: 10.1088/1674–4527/17/12/125

http://www.raa-journal.org *http://iopscience.iop.org/raa*

***R**esearch in*
***A**stronomy and*
***A**strophysics*

A 95 GHz methanol emission survey toward eight small supernova remnants

Ying-Jie Li[1,2], Ye Xu[1], Xi Chen[3,4], Deng-Rong Lu[1], Yan Sun[1], Xin-Yu Du[1,5] and Zhi-Qiang Shen[4]

[1] Purple Mountain Observatory, Chinese Academy of Sciences, Nanjing 210008, China; *xuye@pmo.ac.cn*
[2] University of Science and Technology of China, Chinese Academy of Sciences, Hefei 230026, China; *liyj@pmo.ac.cn*
[3] Center for Astrophysics, Guangzhou University, Guangzhou 51006, China; *chenxi@shao.ac.cn*
[4] Shanghai Astronomical Observatory, Chinese Academy of Sciences, Shanghai 200030, China
[5] University of the Chinese Academy of Sciences, Beijing 100049, China

Abstract We report on a 95 GHz ($8_0 - 7_1$ A$^+$) methanol (CH_3OH) emission survey with the Purple Mountain Observatory Delingha 13.7 m telescope. Eight supernova remnants (SNRs) with angular size $\lesssim 10'$ were observed, but emission was only detected in three SNRs near the Galactic center (Sgr A East, G 0.1–0.1 and G 359.92–0.09). CH_3OH emission mainly surrounds the SNRs and can be decomposed into nine spatial peaks with the velocity range of eight peaks being $(-30, 70)$ km s^{-1}, and the other is $(70, 120)$ km s^{-1}. They are probably excited by interaction with these SNRs and adjacent molecular gas in the central molecular zone (CMZ), although star formation may play an important role in exciting CH_3OH emission in some regions of CMZ. We infer that tidal action is unlikely to be an excitation source for CH_3OH emission.

Key words: ISM: molecules — ISM: supernova remnants — Galaxy: center — ISM: kinematics and dynamics — ISM: clouds

1 INTRODUCTION

The methanol molecule (CH_3OH) is a slightly asymmetric top with hindered internal rotation. It processes a multitude of allowed radio transitions. CH_3OH in space has been actively studied since its discovery by Ball et al. (1970); abundant CH_3OH transitions have been detected at sub-millimeter and millimeter wavelengths, and are sensitive to the density and kinetic temperature of dense clouds (see e.g., Menten et al. 1988b,a; Leurini et al. 2004, and references therein). CH_3OH is one of the most abundant complex molecules in star formation regions (Kalenskii et al. 1997), where both its thermal (Slysh et al. 1994; Hatchell et al. 1998) and maser (see below) lines can trace star formation activities. However, for CH_3OH lines at 95 GHz ($8_0 - 7_1$ A$^+$), the attention has mostly been concentrated on its maser (belonging to class I CH_3OH maser lines) emission, though there are a few detections of thermal emission as well (see e.g., Val'tts et al. 2000; Chen et al. 2012).

Class I CH_3OH maser lines that are pumped by collisions, such as at 36 GHz ($4_{-1} - 3_0$ E), 44 GHz ($7_0 - 6_1$ A$^+$), 95 GHz ($8_0 - 7_1$ A$^+$), etc., have long been assumed to be associated with both low-mass and high-mass star formation (Kalenskiĭ et al. 2006; Chen et al. 2011; Yang et al. 2017). From the beginning of 2011, targeted searches for these masers toward supernova remnants (SNRs) began to be carried out (Litovchenko et al. 2011). These maser emissions, such as at 36 GHz ($4_{-1} - 3_0$ E) and 44 GHz ($7_0 - 6_1$ A$^+$), have been detected in some SNRs (Litovchenko et al. 2011; Pihlström et al. 2011, 2014). However, there is only one detection of the 95 GHz CH_3OH maser line in an SNR (i.e., SNR Kes 79, Zubrin & Shulga 2008), and it is controversial in that Frail (2011) claimed that the 12 m Arizona Radio Observatory failed to confirm this detection. The CH_3OH maser line at 95 GHz is excited under a stricter range of conditions than that at 36 and 44 GHz (see e.g., McEwen et al. 2014; Nesterenok 2016). That may be the factor causing fewer 95 GHz CH_3OH maser emissions to be de-

tected in SNRs. This factor may also be due to not having a large survey of SNRs at 95 GHz. We are interested in whether CH_3OH emission is associated with SNRs.

Yusef-Zadeh et al. (2013) explained the enhanced abundance of CH_3OH in the Galactic center in terms of the interaction between cosmic rays and molecular gas, which produces γ-rays (Frail 2011). Therefore, the presence of γ-ray emission such as at GeV or TeV energies marks a possibility of enhanced abundance of CH_3OH (such as at 36, 44 and 95 GHz), and hence may raise the possibility of detection. Although the excitation conditions for these three masers are different, all three maser emission outputs are presented over a wide range of environments (see e.g., McEwen et al. 2014; Leurini et al. 2016). In order to expect a high detection rate and save time, the selection criteria are that the SNRs are small ($\lesssim 10'$) and associated with a class I methanol 36/44 GHz maser or GeV/TeV emission. We select eight SNRs, with three (Sgr A East, G 0.1–0.1 and G 359.92–0.09) located in the Galactic center.

Table 1 summarizes the physical properties of the selected SNRs, including their interaction with clouds, the occurrence of 1720 MHz OH and a class I methanol 36/44 GHz maser, SNR type and high-energy emission.

We report on a 95 GHz CH_3OH emission survey toward eight SNRs using the Purple Mountain Observatory Delingha (PMODLH) 13.7 m radio telescope. Observation and data reduction are described in Section 2, and the survey outcomes in Section 3. Section 4 discusses whether the 95 GHz CH_3OH emission can be identified as maser lines. In Section 5, we discuss the correlation of 95 GHz CH_3OH emission with SNRs, star formation and tidal action, and why 95 GHz CH_3OH emission was only detected around Sgr A East, G 0.1–0.1 and G 359.92–0.09. Finally, Section 6 summarizes the important results.

2 OBSERVATION AND DATA REDUCTION

Using the PMODLH 13.7 m telescope, the CH_3OH (8_0-7_1 A^+, 95.16949 GHz, hereafter 95 GHz CH_3OH) line was observed toward eight SNRs from 2015 May 5 to June 25. The telescope operates in sideband separation mode, and uses a fast Fourier transform spectrometer (Shan et al. 2012).

Sgr A East, G 0.1–0.1 and G 359.92–0.04 were mapped in a single image spanning a $\sim\ 20' \times 20'$ (49.5 pc^2 at 8.5 kpc) cell (we denote this region the Galactic central SNRs region, GCSNRR), and the remaining five SNRs were mapped in $10' \times 10'$ cells (see Table 2). We used the on-the-fly observational mode with a constant rate of $50'' \, s^{-1}$ along lines in R.A. and Decl. directions on the sky. The receiver recorded spectra every 0.3 s. The standard chopper wheel method was used for calibration (Penzias & Burrus 1973; Ulich & Haas 1976). The half-power beam width of the telescope was approximately $58''$ at 95 GHz. Typical system temperature, $T_{\rm sys}$, during the observations was $160 - 190$ K. Antenna temperatures, $T_{\rm A}^*$, were calibrated to the main beam temperatures, $T_{\rm R}^*$, with main beam efficiency $\eta_{\rm mb}$ = 62%. The calibrated data were re-gridded to $30''$ pixels. Table 2 summarizes mapping the center and main beam root mean square noise (RMS) per 61 kHz channel (corresponding to 0.19 km s^{-1} at 95 GHz) for each target source.

3 RESULTS

The survey resulted in three detections (Sgr A East, G 0.1–0.1 and G 359.92–0.09) that are covered by GCSNRR. We focused on the general distribution of 95 GHz CH_3OH emission in GCSNRR in this section.

Figure 1 shows a 95 GHz CH_3OH integrated intensity map, where Sgr A* is indicated by a blue filled pentagram. The 95 GHz CH_3OH emission south of Decl.$\sim$–29°02′ shows two distinct velocity components. We integrated the emission separately over the low velocity component, -30 to 70 km s^{-1} (Fig. 1, the left panel), and high velocity component, 70 to 120 km s^{-1} (Fig. 1, right panel).

Nine spatial peaks are evident, as shown in Figure 1 by diamonds, and listed in Table 3. Only one position, located in the southwestern region of the map, contains two peaks, corresponding to peak 8 for the low velocity gas (Fig. 1, left panel) and peak 9 for the high velocity gas (Fig. 1, right panel). Peak 9, where velocity is centered at $\sim$ 85 km s^{-1}, is much weaker with integral intensity of 0.47 K km s^{-1}. Figure 1 also indicates that most 95 GHz CH_3OH emission surrounds SNRs. The correlation between them will be discussed in Section 5.1.

Figure 2 presents the spectra of the nine emission peaks. The spectrum of peak 4 shows a bimodal structure. For peak 5, the spectrum shows a possible second velocity component centered at $\sim$45 km s^{-1}, where the peak T_R^* of this component is less than 3 $\times$ RMS. The spectrum of peak 7 indicates a second velocity component centered at $\sim$85 km s^{-1}, which surrounds peak 9, as is apparent from the spatial distribution (see the right

Table 1 SNR Properties

Name	Interacting with molecular clouds[1]	OH 1720 MHz maser[a]	CH_3OH 36/44 GHz maser[b]	Type	X-ray	GeV Flux[c] (10^{-9} ph cm^{-2} s^{-1})	TeV[2] (σ)
(1)	(2)	(3)	(4)	(5)	(6)	(7)	(8)
Sgr A East	Y	Y	Y	TC[d]	Y[e]	65.02	HESS (66.6)
G 0.1–0.1	Y?			C?[f]	Y[g]	1.0[3]	HESS (11.5)
G 1.4–0.1	Y	Y	Y	S[h]		0.4[3]	HESS (6.5)
G 29.7–0.3	Y	Y	N	C[i]	Y[j]	2.1[3]	HESS (10.1)
G 111.7–2.1	Y?	N		S[k]	Y[l]	6.25	MAGIC (5.2)
G 120.1+1.4	Y?	N		S[m]	Y[l]	2.1[3]	VERITAS (5.8)
G 184.6–5.8	?			F[n]	Y[l]	108.12	HESS (129)
G 359.92–0.09[4]	Y[o]						

Notes: (a) Frail et al. (1996); Koralesky et al. (1998); Yusef-Zadeh et al. (1999); Davies et al. (2009); (b) Litovchenko et al. (2011); Pihlström et al. (2011, 2014); (c) Acero et al. (2016); (d) Yusef-Zadeh et al. (2003); Vink (2012); (e) Maeda et al. (2002); (f) Heard & Warwick (2013); (g) Yusef-Zadeh et al. (2002b); (h) Frail (2011); (i) Becker et al. (1983); Blanton & Helfand (1996); (j) Sugizaki et al. (2001); (k) Aharonian et al. (2001); Albert et al. (2007); (l) Predehl & Schmitt (1995); (m) Acciari et al. (2011); (n) Wallace et al. (1994, 1999); (o) Coil & Ho (2000); Herrnstein & Ho (2005); Amo-Baladrón et al. (2011). In the column of "Type", S=shell, C=composite, F=plerion, TC=thermal composite (i.e. mixed-morphology), C?=probably thermal & plerionic composite. In the other columns, Y=yes, N=no, Y?=probable, ?=possible, Null=no data. (1) See "A List of Galactic SNRs Interacting with Molecular Clouds", and references therein (*http://astronomy.nju.edu.cn/ỹgchen/others/bjiang/interSNR6.htm*). (2) This column includes TeV γ-ray detections by experiment and significance of detection in parentheses for HESS (Aharonian et al. 2006, 2008; Bochow 2011), MAGIC (Albert et al. 2007) and VERITAS (Acciari et al. 2011). (3) Upper limits of flux with 99% confidence and PL index $\Gamma = 2$, see table 3 in Acero et al. (2016). (4) This SNR is neither included in "A census for high-energy-observations of Galactic supernova remnants" (*http://www.physics.umanitoba.ca/snr/SNRcat/*, Ferrand & Safi-Harb 2012) nor in "A catalogue of Galactic supernova remnants" (*http://www.mrao.cam.ac.uk/surveys/snrs/*, Green 2014).

Table 2 Observed SNR Positions and Observing RMS

Region	R.A. (J2000)	Dec. (J2000)	Size (arcmin)	RMS (mK)
GCSNRR[1]	17 45 44.0	–29 00 00	20	25
G 1.4–0.1	17 49 39.0	–27 46 00	10	25
G 29.7–0.3	18 46 25.0	–02 59 00	10	39
G 111.7–2.1	23 23 26.0	58 48 00	10	28
G 120.1+1.4	00 25 18.0	64 09 00	10	29
G 184.6–5.8	05 34 31.0	22 01 00	10	27

Notes: The columns show the name, mapping center in equatorial coordinates (J2000), mapping size and RMS per channel of each region.
(1) This region covers SNRs Sgr A East, G 0.1–0.1 and G 359.92–0.09.

Table 3 Peak Emission for 95 GHz CH_3OH

Peak ID	R.A. (J2000)	Dec. (J2000)	Velocity (km s^{-1})	Integrated intensity (K km s^{-1})
peak 1	17:45:52.0	–28:51:30	49.9	0.92
peak 2	17:46:10.3	–28:53:30	53.0	4.80
peak 3	17:45:52.0	–28:55:30	46.7	0.59
peak 4	17:46:03.4	–28:55:30	47.0	1.93
peak 5	17:45:52.0	–28:56:30	–6.4	0.52
peak 6	17:45:52.0	–28:59:00	43.2	10.94
peak 7	17:45:38.3	–29:03:30	18.8	3.73
peak 8	17:45:36.0	–29:06:00	6.8	2.65
peak 9	17:45:36.0	–29:06:00	84.8	0.47

Notes: The fourth column is the intensity weighted velocity (moment 1). The last column is integrated intensity which is integrated over velocity from -30 to 70 km s^{-1} for peaks $1-8$, and from 70 to 120 km s^{-1} for peak 9.

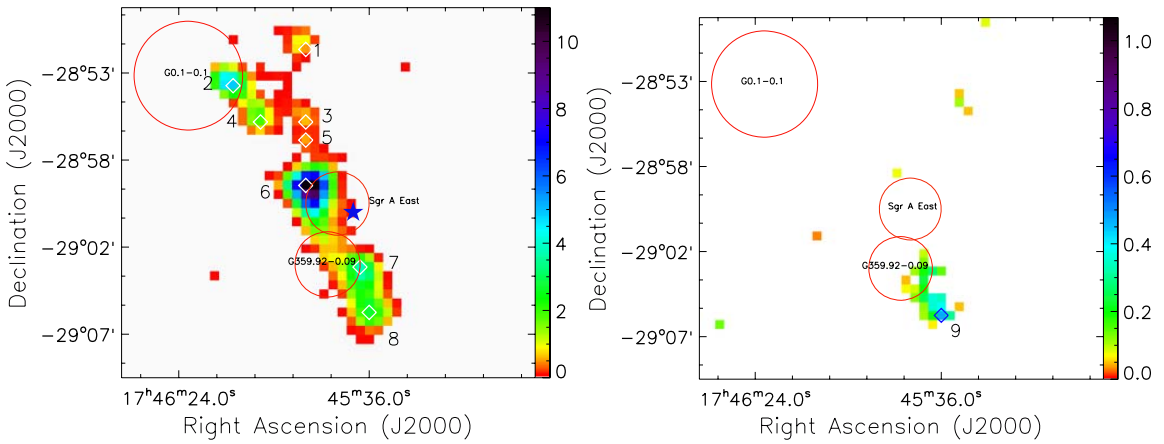

Fig. 1 Integrated intensity maps of 95 GHz CH_3OH, integrated over -30 to 70 km s^{-1} (*left*) and 70 to 120 km s^{-1} (*right*). Color bar units are K km s^{-1}. Maximum integral intensity of 95 GHz CH_3OH in the left and right panels are 10.94 and 0.47 K km s^{-1}, and the scales are 11.0 and 1.1 K km s^{-1}, respectively. The blue filled pentagram indicates the position of Sgr A*. The diamonds show peak positions. The red circles indicate SNRs. The circles indicating G 359.92–0.09 and Sgr A East are the real angular size. The size of SNR G 0.1–0.1 is uncertain.

panel of Fig. 1). The spectra of the remaining peaks are centrally dominated.

Figure 3 shows the velocity (intensity weighted, i.e., moment 1) structure of the entire region for both the low (left panel) and high velocity (right panel) components. A significant velocity gradient from the southwest to northeast is evident in both panels. Velocities for the low velocity component (left panel) vary from $\sim$10 to $\sim$60 km s^{-1}, and from $\sim$80 to $\sim$100 km s^{-1} for the high velocity component (right panel).

Figure 4 shows the position-velocity map along the black arrow marked in Figure 3. The peak emission is centered at $\sim$ 45 km s^{-1}. There is also a variation of velocities from $\sim$ 10 to $\sim$60 km s^{-1} from the southwest to northeast, with corresponding velocity gradient $\sim$2 km s^{-1} pc^{-1}. The velocity gradient decreases when the position passes $\sim$0.20°. There is a similar velocity gradient for the high velocity component (position ranges from $\sim$0.02° to 0.12°), but the emission is much weaker.

4 IS 95 GHZ CH_3OH EMISSION MASER EMISSION?

Similar to previous work toward the vicinities of Sgr A and Sgr B2 (Val'tts et al. 2000), the broad line profiles in Figure 2 suggest that thermal emission contributes significantly to the detections.

The distribution of 95 GHz CH_3OH emission is concentrated. In order to avoid the emission peaks being divided by pixels, the central zone is assumed to contain four pixels, i.e., 1′ square. The central zone peak intensity is much higher than the pixels outside it. For peaks 1–5, integrated intensities outside the central zone are $\lesssim 60\%$ of the central zone peak intensity. This implies that peak intensities arise from compact areas, i.e., the emission has limited spatial extent, which indicates that maser emission may make a contribution to the total 95 GHz CH_3OH emission in peaks 1–5.

The 95 GHz CH_3OH maser originates in the same clump of gas that produces the 36 and 44 GHz CH_3OH masers (Plambeck & Menten 1990). Figure 5 indicates that the 95 GHz CH_3OH emission correlates with the 36/44 GHz CH_3OH maser emission in some regions, and most of those co-location regions are around or in peaks 6–8. This also indicates that part of the 95 GHz CH_3OH emission may be maser emission, particularly in regions around or in peaks 6–8. The velocities of 36/44 GHz CH_3OH masers in Figure 5 are less than 60 km s^{-1}, so we did not compare these with the high velocity component of 95 GHz CH_3OH emission.

Thus, there may be a small fraction of 95 GHz CH_3OH maser emission buried within thermal emission, and higher resolution and sensitivity observations would help to confirm this speculation.

5 EXCITATION SOURCE FOR 95 GHZ CH_3OH EMISSION

In this section, we extend peaks to clouds that are distinguishable from each other and clearly cover the corresponding peaks, and number clouds accordingly (e.g., cloud 1 corresponds to peak 1). We discuss the possible

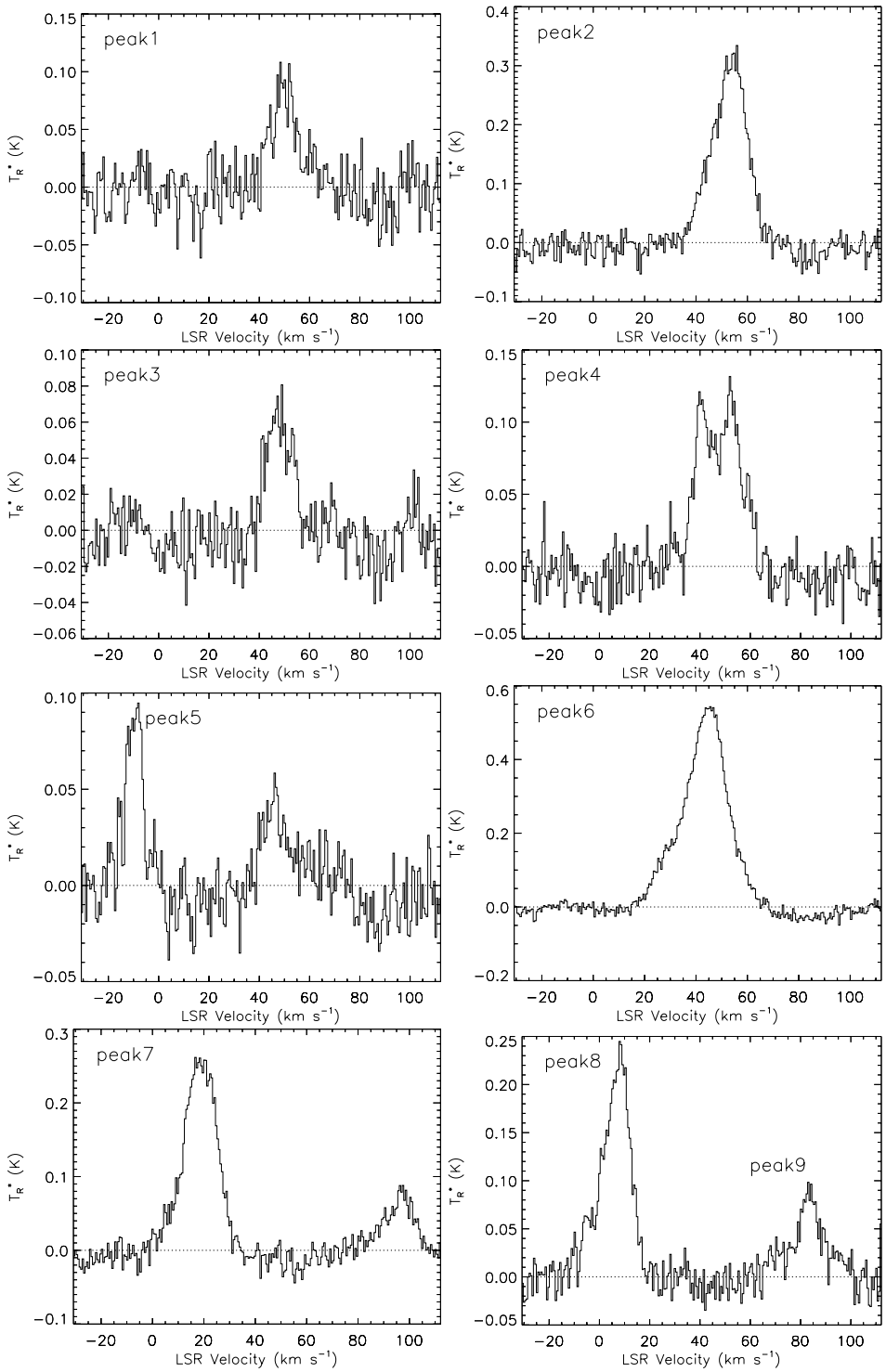

Fig. 2 Spectra of peaks from Table 3. Spectra are averaged over three velocity channels.

excitation sources for 95 GHz CH_3OH emission. Surveys have revealed that class I methanol masers, such as 36 and 44 GHz methanol masers, are associated with not only star formation (Kalenskii et al. 2010; Chen et al. 2012), but also SNRs (Litovchenko et al. 2011; Pihlström et al. 2011, 2014). To investigate which one dominates the excitation for 95 GHz CH_3OH emission in GCSNRR, we combine data of 20 cm continuum emission, 36 GHz CH_3OH and 1720 MHz OH maser emission, HII regions and WISE data. We also discuss the influence of tidal ac-

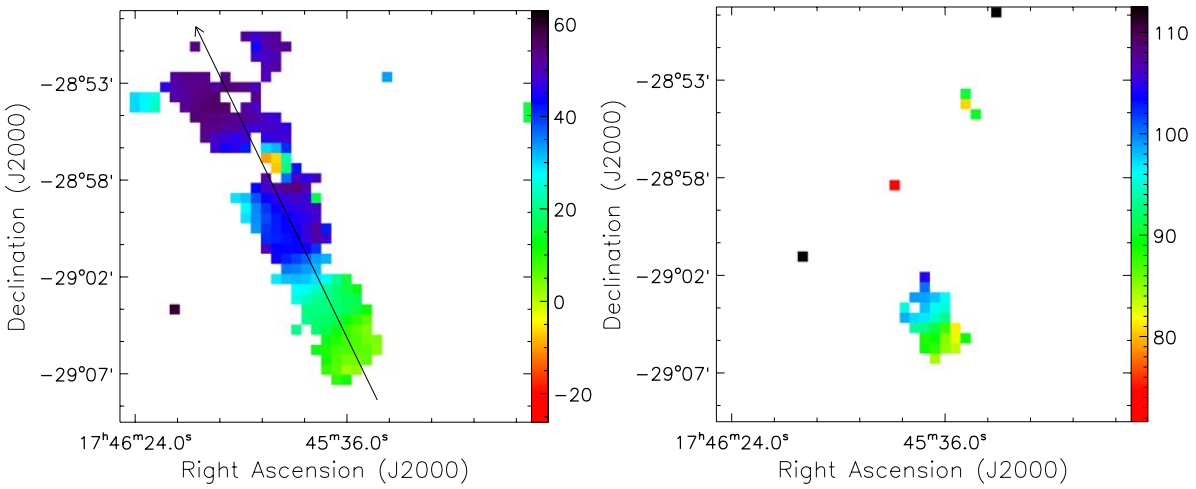

Fig. 3 Velocity maps of 95 GHz CH_3OH. Color bar units are km s^{-1}. Color images show the intensity weighted velocity (moment 1), $V_{\rm lsr}$, distribution of 95 GHz CH_3OH. The left and right panels show the velocity distribution of low $(-30, 70)$ km s^{-1} and high $(70, 120)$ km s^{-1} velocity components, respectively. The scales of the left and right panels are $(-30, 70)$ and $(70, 120)$ km s^{-1}, respectively. The long black arrow in the left panel indicates the axis of the position-velocity map shown in Fig. 4.

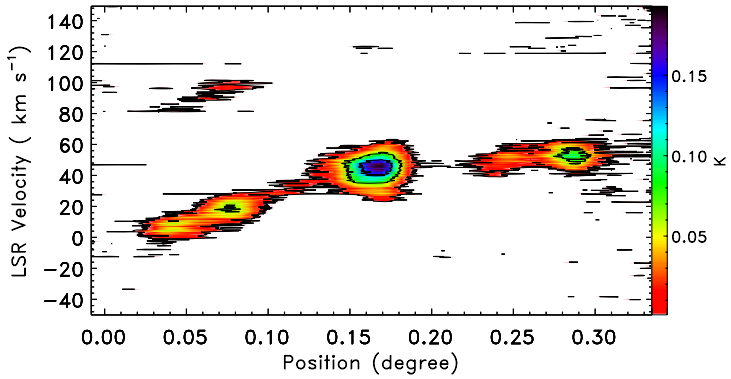

Fig. 4 Position-velocity map of 95 GHz CH_3OH along the arrow shown in Fig. 3. Spectra at each position are averaged over 5′ perpendicular to the axis; 0.00° on the x-axis corresponds to (R.A., Decl.) = ($17^{\rm h}45^{\rm m}29.1^{\rm s}$, –29°08′ 30″; and 0.34° to (R.A., Decl.) = ($17^{\rm h}46^{\rm m}10.3^{\rm s}$, $-28°50'00''$). Contour levels are 15%, 45% and 75% of the maximum value (0.19 K).

tion, because GCSNRR is close to the Galactic center. We also discuss why 95 GHz CH_3OH emission is only detected in GCSNRR. A summary is given at the end of this section.

5.1 Interaction between 95 GHz CH_3OH Emission and SNRs

5.1.1 Relative Position among 95 GHz CH_3OH Emission and SNRs or a Superbubble

The 5 GHz and 20 cm continuum emission can trace both HII regions and SNRs in the vicinity of Sgr A East (Serabyn et al. 1992; Yusef-Zadeh et al. 2004). For example, there are distinct differences in the 20 cm continuum emission map between HII regions (Yusef-Zadeh et al. 2004, figures 19b, 21a and 23b) and SNRs (Yusef-Zadeh et al. 2004, figures 19b and 21a). We use the 20 cm continuum emission map to identify SNRs.

Figure 6 shows the 95 GHz CH_3OH emission contours superimposed on the 20 cm radio continuum emission image from Yusef-Zadeh et al. (2004). To show the 20 cm radio continuum emission more explicitly, the two images have different maximal values: the left panel $= 4.5$ Jy beam^{-1} and the right panel $= 1.0$ Jy beam^{-1}.

The blue circle in Figure 6 indicates a superbubble candidate, G 359.9–0.125, centered at $(l, b) \sim (359.84°, -0.14°)$ with size $15' \times 3'$ (Mori et al. 2008; Ponti et al. 2015, and references therein). The red circles indicate three SNRs: Sgr A East, G 0.1–0.1 and G 359.92–0.09. SNR Sgr A East is clear in the left panel,

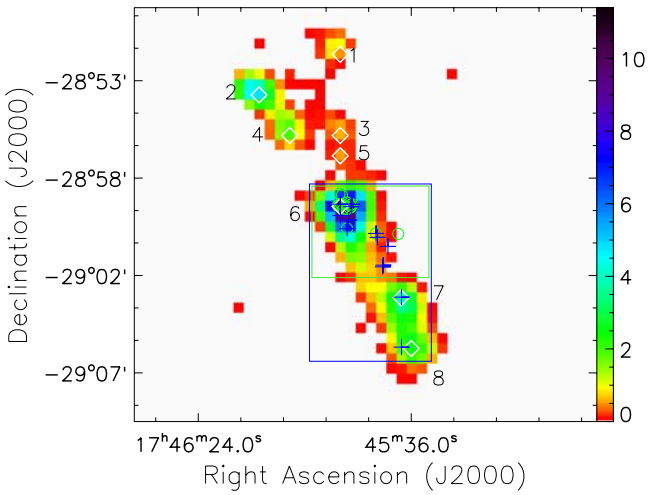

Fig. 5 Relative positions of the 36 GHz CH_3OH masers (*blue pluses*; Liechti & Wilson 1996; Sjouwerman et al. 2010, and references therein), 44 GHz CH_3OH masers (*green open circles*; Pihlström et al. 2011, and references therein) and 95 GHz CH_3OH emission (color image, integrated over -30 to 70 km s^{-1}, the scale is 10.6 K km^{-1}). Color bar units are K km s^{-1}. The blue and green rectangles indicate the study regions of 36 and 44 GHz CH_3OH masers in those references, respectively.

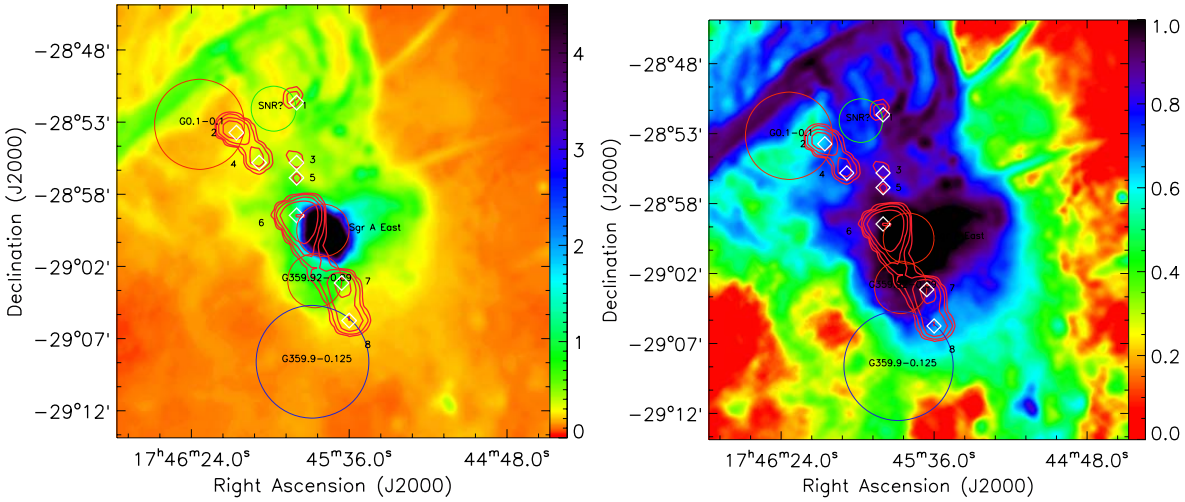

Fig. 6 Contours of 95 GHz CH_3OH emission between -30 and 70 km s^{-1} superimposed on the 20 cm radio continuum image from Yusef-Zadeh et al. (2004). Contours start at 3σ and increase in steps of 1, 2, 4, 8 and $16\times3\sigma$, where $\sigma = 0.11$ K km s^{-1}. Color bar units are Jy beam^{-1}, and the scales of the left and right panels are 4.5 and 1.0 Jy beam^{-1}, respectively. The *red* circles indicate SNRs, the *green* circle indicates an SNR candidate (marked as "SNR?"), and the *blue* circle indicates a superbubble candidate. The circles indicating G 359.92–0.09 and Sgr A East are the real angular size, and that of G 359.9–0.125 is half the real angular size. The sizes of SNR G 0.1–0.1 and "SNR?" are uncertain. The diamonds indicate peak positions, and contours outline clouds.

and the right panel probably shows a shell-like structure in the vicinity of cloud 1. This shell-like structure may indicate an SNR candidate located at R.A. $\sim17^{\rm h}46^{\rm m}00^{\rm s}$, Decl. $\sim-28°52'12''$; and represented by a green circle marked with "SNR?".

Cloud 1 lies toward the northwest of the SNR candidate. Clouds 2 and 4 are toward the southwest of the SNR G 0.1–0.1 and located in molecular cloud G 0.13–0.13. They are probably interacting with G 0.1–0.1 just as G 0.13–0.13 does (Yusef-Zadeh et al. 2002a). The ridge connecting clouds 6, 7 and 8 (i.e., Mol. Ridge or Molecular Ridge in Herrnstein & Ho 2005; Amo-Baladrón et al. 2011) surrounds the eastern edge of Sgr A East. SNR G 359.92–0.09, which is located to the east of them, probably has a strong interaction with Sgr A East and the eastern edge of the 20 km s^{-1} cloud (Coil & Ho 2000; Herrnstein & Ho 2005; Amo-Baladrón et al. 2011), where clouds 7 and 8 are located. The southeast

of clouds 8 and 9 (the position of peak 9 overlaps with peak 8, see Fig. 1) may interact with superbubble candidate G 359.9–0.125, as shown in Figure 6. Most of the 95 GHz CH_3OH emission surrounds SNRs (Fig. 6), which suggests that the emission may be excited by interaction with SNRs.

5.1.2 Line Widths of 95 GHz CH_3OH *Emission Versus SNRs or a Superbubble*

Molecular line widths can be broadened by interaction between shock and molecular cloud (Kilpatrick et al. 2014). Furthermore, line broadenings are regarded as strong kinematic evidence for the interaction between SNR and molecular cloud (Jiang et al. 2010; Kilpatrick et al. 2016, and references therein). For instance, the broad CS (1–0) line widths are used to indicate the interaction between the Sgr A East shell and the 50 km s^{-1} molecular cloud (Tsuboi et al. 2009). Therefore, 95 GHz CH_3OH line width broadening may be an indicator of interaction among SNRs and 95 GHz CH_3OH clouds.

Figure 7 shows the distribution of line widths for 95 GHz CH_3OH emission. The line for the high velocity component is randomly distributed in the region around peak 9, and therefore omitted in Figure 7.

Figure 7 shows four interesting regions marked by rectangles:

Region A. Line widths relatively higher than their neighborhoods show a reversed-S structure crossing the interface between clouds 7 and 8. In this region, the north part of the reversed-S structure is located west of cloud 7, possibly indicating an interaction among cloud 7, SNR G 359.92-0.09 and Sgr A East. The midsection of the reversed-S structure may indicate SNR G 359.92–0.09 rushing toward cloud 8, or may trace an interaction between clouds 7 and 8. The south part of the reversed-S structure lies south of cloud 8, which may indicate an interaction between cloud 8 and superbubble candidate G 359.9–0.125.

Region B. Line widths in cloud 6 (typical value is $\sim$20 km s^{-1}) are much higher than in other regions, and increase toward the east. This possibly indicates that the 50 km s^{-1} cloud (including cloud 6) has a strong interaction with Sgr A East.

Region C. Line widths increase toward the southeast of cloud 4 and west of cloud 2, which constitute a faint shell. This may suggest an interaction between the 95 GHz CH_3OH cloud and SNR G 0.1–0.1.

Region D. Line widths are higher in the northeast of cloud 1, which may indicate that cloud 1 is interacting with an SNR candidate as discussed above to the east of cloud 1 (see the green circle in the right panel of Figs. 6 and 7). This emission may also be excited by star formation as discussed in Section 5.2.

Figure 7 also shows that 95 GHz CH_3OH line widths are associated with the 36 GHz CH_3OH masers in the south of Decl. $\sim$–28°58′ and 1720 MHz OH masers around Sgr A East. The geometry of the 36 GHz masers in Sgr A East outlines the current location of an SNR shock front (Sjouwerman & Pihlström 2012). Most 1720 MHz OH masers arise in regions where the SNR Sgr A East is interacting with the 20 and 50 km s^{-1} molecular clouds and the nearby SNR G 359.92–0.09 (Sjouwerman & Pihlström 2008). The 50 km s^{-1} molecular cloud includes cloud 6, and the 20 km s^{-1} molecular cloud includes clouds 7 and 8.

As a summary of this subsection, 95 GHz CH_3OH emission may be excited by interaction with SNRs and its line width is probably a good tracer of SNRs.

5.2 Effect of Star Formation

The 95 GHz CH_3OH emission is usually assumed to be associated with star formation (Chen et al. 2011; Yang et al. 2017). HII regions and WISE data are used to indicate star formation regions in this study.

Figure 8 superimposes the positions of HII regions (yellow crosses, adopted from Goss et al. 1985; Kuchar & Clark 1997; Paladini et al. 2003; Anderson et al. 2014, and reference therein) on the WISE false color map, along with the 95 GHz CH_3OH emission contours. Both the HII regions and the WISE emission show that 95 GHz CH_3OH emission deviates slightly from the star formation regions.

The region, where star formation is most likely to be the dominant excitation source for 95 GHz CH_3OH emission in GCSNRR, is cloud 1, because the nearest HII region lies just 0.40′ west of peak 1. The WISE emission also shows that star formation probably plays an important role in exciting CH_3OH emission in clouds 2–5.

Star formation may not be the dominant factor that excites 95 GHz CH_3OH emission in the 50 km s^{-1} cloud (including cloud 6), because the energy restored in the star formation process may be less than the kinetic energy in the 50 km s^{-1} cloud. Specifically, the energy restored in protostellar outflows is up to 10^{47}–10^{48} erg (Bachiller 1996; Livio 2000). That is far less than the ki-

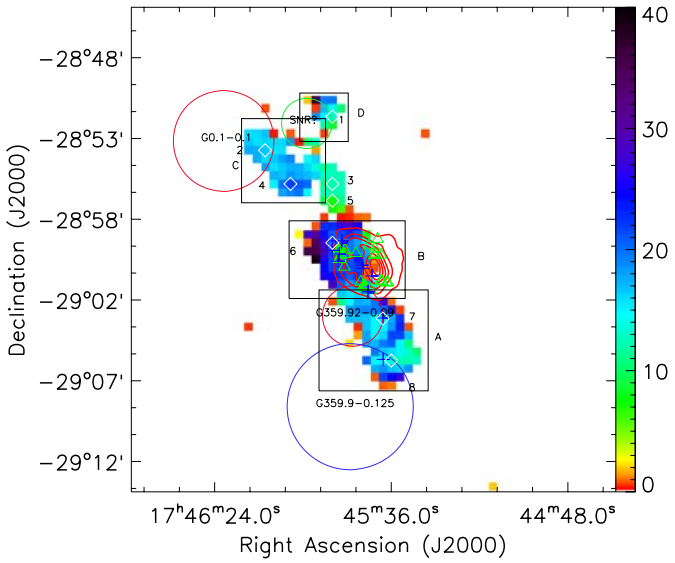

Fig. 7 Distribution of 95 GHz CH_3OH line widths (color image). Maximum is 38.54 km s^{-1}. Color bar units are km s^{-1}. Red contours of the 20 cm continuum image (Yusef-Zadeh et al. 2004) show Sgr A East. The lowest contour level and contour interval are 15% of the maximum (11.23 Jy $beam^{-1}$). Green triangles indicate 1720 MHz OH masers (see Sjouwerman & Pihlström 2008, and references therein), and blue pluses indicate 36 GHz CH_3OH masers (Liechti & Wilson 1996; Sjouwerman et al. 2010, and references therein). The four rectangles highlight four interesting regions.

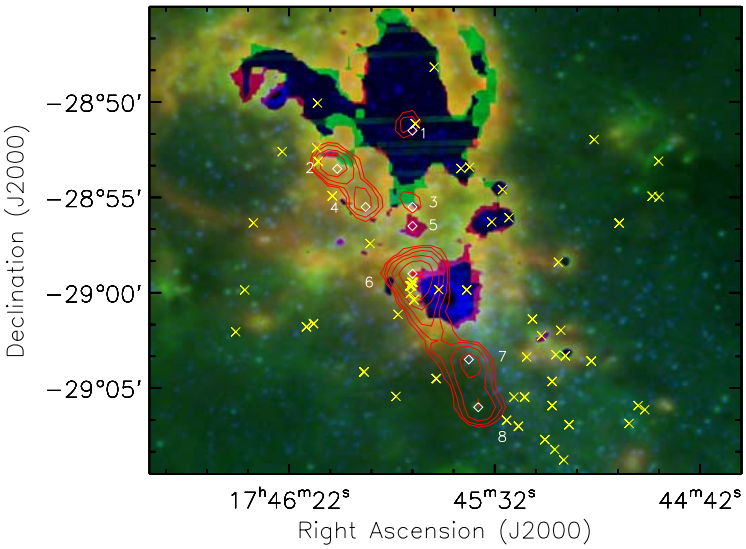

Fig. 8 Background false color map, where blue is the WISE 4.6 μm data, green is 12 μm data and red is 22 μm data, with 95 GHz CH_3OH emission contours between −30 and 70 km s^{-1} and HII regions superimposed (yellow crosses, adopted from Goss et al. 1985; Kuchar & Clark 1997; Paladini et al. 2003; Anderson et al. 2014, and references therein). Contours start at 3σ and increase in steps of 1, 2, 4, 8 and $16\times3\sigma$, where $\sigma = 0.11$ K km s^{-1}. The diamonds indicate peak positions, and contours outline clouds.

netic energy in the 50 km s^{-1} cloud ($0.5m\cdot\Delta V^2 \sim 10^{50}$ erg), where its mass, m, is $\sim 5\times10^4\ M_\odot$ (Herrnstein & Ho 2005) and line width, ΔV, in terms of CH_3OH $\sim$ 20 km s^{-1} (no less than 10 km s^{-1}). Therefore, SNR Sgr A East is more likely to be the dominant excitation source than star formation in the 50 km s^{-1} cloud (including cloud 6).

In clouds 7–9, both HII regions and WISE emission deviate from 95 GHz CH_3OH emission, which suggests that star formation is probably not the dominant excitation source in clouds 7–9.

5.3 Influence of Tidal Action

The Roche density $n_{\rm RL}$ is given by (Mapelli & Gualandris 2016)

$$n_{\rm RL} \sim 10^7\,{\rm cm^{-3}} \left(\frac{m_{\rm BH}}{3\times10^6\,M_\odot}\right)\left(\frac{\rm pc}{r}\right)^3, \quad (1)$$

where $m_{\rm BH} = (4.30 \pm 0.20_{\rm stat} \pm 0.30_{\rm sys}) \times 10^6\,M_\odot$ is the mass of the supermassive black hole (Gillessen et al. 2009; Mapelli & Gualandris 2016), and r is the distance of the molecular cloud from the supermassive black hole. Clouds 6–8 are located in the 20 or 50 km s^{-1} clouds, which are $\sim$ 20pc from the supermassive black hole Sgr A* (Mapelli & Gualandris 2016). Then $n_{\rm RL}$ is no less than 1.8×10^6 cm^{-3}, which is much higher than the number densities in 20 and 50 km s^{-1} clouds (0.4–4×10^5 cm^{-3}, see table 3 of Amo-Baladrón et al. 2011). This indicates that the 20 and 50 km s^{-1} clouds are currently being tidally disrupted according to Mapelli & Gualandris (2016), which is also suggested by Herrnstein & Ho (2005).

Assuming a near equatorial and near-circular orbit about Sgr A*, the tidal potential, $V_{\rm tidal}$, can be estimated as (Murray & Dermott 2000)

$$V_{\rm tidal} = \frac{Gm_{\rm BH}}{4a^3}R^2(3\cos\psi+1), \quad (2)$$

where a and R are the distance of the 50 km s^{-1} cloud from the black hole and the radius of the black hole, respectively, and ψ is the angle between the projected radius vector and the plane perpendicular to the link line between the center of the 50 km s^{-1} cloud and the black hole. Even if $a = R = 0.04$ pc, where 0.04 pc is the upper limit on the radius of the black hole (Amo-Baladrón et al. 2011), $V_{\rm tidal} \sim 10^{18}$ erg, which is far less than the kinetic energy in the 50 km s^{-1} cloud (i.e., $\sim 10^{50}$ erg, see Sect. 5.2). That indicates that tidal action is not likely to be a source that excites CH_3OH emission, although the estimate above is quite approximate. A similar conclusion applies to the 20 km s^{-1} cloud.

5.4 The Role of Cosmic Rays

Observing 36 GHz CH_3OH in the central molecular zone (CMZ, which covers GCSNRR), Yusef-Zadeh et al. (2013) explained the enhanced abundance of CH_3OH in terms of interactions between cosmic rays and molecular gas. Since 95 GHz CH_3OH emission is associated with 36 GHz CH_3OH emission (see Figs. 5 and 7), the 95 GHz CH_3OH emission can be enhanced by these interactions in CMZ.

5.5 The Possible Reason Why 95 GHz CH_3OH Emission Was Only Detected in GCSNRR

Table 1 lists properties of the eight SNRs, and in particular indicates that the type of SNR is a unique character of SNRs Sgr A East and G 0.1–0.1 with the detection of 95 GHz CH_3OH emission. SNR G 0.1–0.1 and Sgr A East are probably thermal and plerionic composite (Heard & Warwick 2013) and thermal composite (Yusef-Zadeh et al. 2003; Vink 2012) SNRs, respectively.

Thermal composite SNRs have interior thermal X-ray emission, and are also known as mixed morphology SNRs (MM SNRs). Frail et al. (1996) and Green et al. (1997) first noted that OH (1720 MHz) SNRs (SNRs where 1720 MHz OH masers have been detected) belonged predominantly to a particular class of MM SNRs that have center-filled thermal X-ray emission. This hypothesis was verified on a firmer statistical footing by Yusef-Zadeh et al. (2003). Interactions between the SNR and associated molecular cloud play an important role in producing this interior X-ray gas (Frail 2011). The 95 GHz CH_3OH emission in cloud 6 is associated with 1720 MHz OH maser emission, which also supports a possible correlation between SNR type and 95 GHz CH_3OH emission. This correlation could also be one of the possible reasons why 95 GHz CH_3OH emission was only detected in GCSNRR.

On the other hand, interaction between cosmic rays and molecular gas may be another reason why 95 GHz CH_3OH emission was only detected in GCSNRR. Cosmic rays colliding with ambient gas produce γ-rays (Frail 2011), such as GeV/TeV emission. The region surrounding the Galactic center is among the brightest and most complex in high-energy γ-rays (Ajello et al. 2016, and references therein). Although both the GeV and TeV fluxes around Sgr A East are less than those in G 184.6–5.8, they are much higher than those in G 1.4–0.1, G 29.7–0.3, G 111.7–2.1 and G 120.1+1.4 (see Table 1). In addition, it is unlikely that SNR G 184.6–5.8 interacts with molecular clouds (Graham et al. 1990; Fish et al. 2007; Kilpatrick et al. 2016). Therefore, the interaction between cosmic rays and molecular gas near the Galactic center could still be one of the possible reasons why 95 GHz CH_3OH emission was only detected in GCSNRR.

As a summary of this section, 95 GHz CH_3OH emission is probably excited by interaction with SNRs and may also correlate with the type of SNR. Although star

formation may play an important role in exciting 95 GHz CH_3OH emission in some regions, it is probably not the dominant excitation source in clouds 7–9, and may not be the dominant excitation source in cloud 6. It is difficult to clarify whether star formation or SNRs are the dominant excitation source in clouds 1–5. Interaction between cosmic rays and molecular gas in CMZ may enhance 95 GHz CH_3OH emission. The contribution from tidal action to exciting 95 GHz CH_3OH emission is negligible. We also suggest that the possible reasons why 95 GHz CH_3OH emission was only detected in GCSNRR may be correlated with the type of SNRs near the Galactic center, and the interaction between cosmic rays and molecular gas in CMZ. However, a larger sample in a future survey is required to confirm the correlation between 95 GHz CH_3OH emission and the type of SNR.

6 SUMMARY

We conducted a survey of 95 GHz ($8_0 - 7_1$ A^+) CH_3OH emission toward eight SNRs with angular size $\lesssim 10'$. The main summaries are as follows:

(1) 95 GHz CH_3OH emission was only detected in Sgr A East, G 0.1–0.1 and G 359.92–0.09. The emission can be decomposed into nine spatial peaks with velocity range of eight peaks being (-30, 70) km s^{-1}, and the other is (70, 120) km s^{-1}.
(2) Part of the 95 GHz CH_3OH emission may be maser emission in some regions, particularly in regions around or in peaks 1–8. Higher resolution and sensitivity observations are required to confirm this speculation.
(3) Most 95 GHz CH_3OH emission surrounds SNRs, and is probably excited by interacting with SNRs in CMZ, although star formation is probably important for exciting 95 GHz CH_3OH emission in some regions of CMZ. The influence of tidal action is negligible.
(4) SNR type and interaction between cosmic rays and molecular gas in CMZ could be possible reasons why 95 GHz CH_3OH emission was only detected toward SNRs near the Galactic center. A larger sample is required to confirm the correlation between 95 GHz CH_3OH emission and the type of SNR.

Acknowledgements We acknowledge Fa-cheng Li, Yuliang Xin, Zhaoqiang Shen and Yuehui Ma for their valuable help, and thank Farhad Yusef-Zadeh for providing the 20 cm radio image. This work was supported by the National Natural Science Foundation of China (Grant Nos. 11673066, 11233007, 11590781 and 11273043), and the Key Laboratory for Radio Astronomy.

References

Acciari, V. A., Aliu, E., Arlen, T., et al. 2011, ApJ, 730, L20
Acero, F., Ackermann, M., Ajello, M., et al. 2016, ApJS, 224, 8
Aharonian, F., Akhperjanian, A., Barrio, J., et al. 2001, A&A, 370, 112
Aharonian, F., Akhperjanian, A. G., Bazer-Bachi, A. R., et al. 2006, A&A, 457, 899
Aharonian, F., Akhperjanian, A. G., Barres de Almeida, U., et al. 2008, A&A, 488, 219
Ajello, M., Albert, A., Atwood, W. B., et al. 2016, ApJ, 819, 44
Albert, J., Aliu, E., Anderhub, H., et al. 2007, A&A, 474, 937
Amo-Baladrón, M. A., Martín-Pintado, J., & Martín, S. 2011, A&A, 526, A54
Anderson, L. D., Bania, T. M., Balser, D. S., et al. 2014, ApJS, 212, 1
Bachiller, R. 1996, ARA&A, 34, 111
Ball, J. A., Gottlieb, C. A., Lilley, A. E., & Radford, H. E. 1970, ApJ, 162, L203
Becker, R. H., Helfand, D. J., & Szymkowiak, A. E. 1983, ApJ, 268, L93
Blanton, E. L., & Helfand, D. J. 1996, ApJ, 470, 961
Bochow, A. 2011, A Systemtatic Study of Supernova Remnants as seen with HESS, PhD Thesis, Ruperto-Carola University of Heidelberg
Chen, X., Ellingsen, S. P., Shen, Z.-Q., Titmarsh, A., & Gan, C.-G. 2011, ApJS, 196, 9
Chen, X., Ellingsen, S. P., He, J.-H., et al. 2012, ApJS, 200, 5
Coil, A. L., & Ho, P. T. P. 2000, ApJ, 533, 245
Davies, B., Origlia, L., Kudritzki, R.-P., et al. 2009, ApJ, 694, 46
Ferrand, G., & Safi-Harb, S. 2012, Advances in Space Research, 49, 1313
Fish, V. L., Sjouwerman, L. O., & Pihlström, Y. M. 2007, ApJ, 670, L117
Frail, D. A. 2011, Mem. Soc. Astron. Italiana, 82, 703
Frail, D. A., Goss, W. M., Reynoso, E. M., et al. 1996, AJ, 111, 1651
Gillessen, S., Eisenhauer, F., Fritz, T. K., et al. 2009, ApJ, 707, L114
Goss, W. M., Schwarz, U. J., van Gorkom, J. H., & Ekers, R. D. 1985, MNRAS, 215, 69P
Graham, J. R., Wright, G. S., & Longmore, A. J. 1990, ApJ, 352, 172

Green, A. J., Frail, D. A., Goss, W. M., & Otrupcek, R. 1997, AJ, 114, 2058
Green, D. A. 2014, Bulletin of the Astronomical Society of India, 42, 47
Hatchell, J., Thompson, M. A., Millar, T. J., & MacDonald, G. H. 1998, A&AS, 133, 29
Heard, V., & Warwick, R. S. 2013, MNRAS, 434, 1339
Herrnstein, R. M., & Ho, P. T. P. 2005, ApJ, 620, 287
Jiang, B., Chen, Y., Wang, J., et al. 2010, ApJ, 712, 1147
Kalenskii, S. V., Dzura, A. M., Booth, R. S., Winnberg, A., & Alakoz, A. V. 1997, A&A, 321, 311
Kalenskiĭ, S. V., Promyslov, V. G., Slysh, V. I., Bergman, P., & Winnberg, A. 2006, Astronomy Reports, 50, 289
Kalenskii, S. V., Johansson, L. E. B., Bergman, P., et al. 2010, MNRAS, 405, 613
Kilpatrick, C. D., Bieging, J. H., & Rieke, G. H. 2014, ApJ, 796, 144
Kilpatrick, C. D., Bieging, J. H., & Rieke, G. H. 2016, ApJ, 816, 1
Koralesky, B., Frail, D. A., Goss, W. M., Claussen, M. J., & Green, A. J. 1998, AJ, 116, 1323
Kuchar, T. A., & Clark, F. O. 1997, ApJ, 488, 224
Leurini, S., Menten, K. M., & Walmsley, C. M. 2016, A&A, 592, A31
Leurini, S., Schilke, P., Menten, K. M., et al. 2004, A&A, 422, 573
Liechti, S., & Wilson, T. L. 1996, A&A, 314, 615
Litovchenko, I. D., Alakoz, A. V., Val'Tts, I. E., & Larionov, G. M. 2011, Astronomy Reports, 55, 978
Livio, M. 2000, Unsolved Problems in Stellar Evolution, 12 (Cambridge: Cambridge University Press)
Maeda, Y., Baganoff, F. K., Feigelson, E. D., et al. 2002, ApJ, 570, 671
Mapelli, M., & Gualandris, A. 2016, in Lecture Notes in Physics, Berlin Springer Verlag, 905, eds. F. Haardt, V. Gorini, U. Moschella, A. Treves, & M. Colpi, 205
McEwen, B. C., Pihlström, Y. M., & Sjouwerman, L. O. 2014, ApJ, 793, 133
Menten, K. M., Reid, M. J., Moran, J. M., et al. 1988a, ApJ, 333, L83
Menten, K. M., Walmsley, C. M., Henkel, C., & Wilson, T. L. 1988b, A&A, 198, 253
Mori, H., Tsuru, T. G., Hyodo, Y., Koyama, K., & Senda, A. 2008, PASJ, 60, S183
Murray, C. D., & Dermott, S. F. 2000, Solar System Dynamics (Cambridge: Cambridge Univ. Press)
Nesterenok, A. V. 2016, MNRAS, 455, 3978
Paladini, R., Burigana, C., Davies, R. D., et al. 2003, A&A, 397, 213
Penzias, A. A., & Burrus, C. A. 1973, ARA&A, 11, 51
Pihlström, Y. M., Sjouwerman, L. O., & Fish, V. L. 2011, ApJ, 739, L21
Pihlström, Y. M., Sjouwerman, L. O., Frail, D. A., et al. 2014, AJ, 147, 73
Plambeck, R. L., & Menten, K. M. 1990, ApJ, 364, 555
Ponti, G., Morris, M. R., Terrier, R., et al. 2015, MNRAS, 453, 172
Predehl, P., & Schmitt, J. H. M. M. 1995, A&A, 293, 889
Serabyn, E., Lacy, J. H., & Achtermann, J. M. 1992, ApJ, 395, 166
Shan, W., Yang, J., Shi, S., et al. 2012, IEEE Transactions on Terahertz Science and Technology, 2, 593
Sjouwerman, L. O., & Pihlström, Y. M. 2008, ApJ, 681, 1287
Sjouwerman, L. O., & Pihlström, Y. M. 2012, in IAU Symposium, 287, Cosmic Masers - from OH to H0, eds. R. S. Booth, W. H. T. Vlemmings, & E. M. L. Humphreys, 449
Sjouwerman, L. O., Pihlström, Y. M., & Fish, V. L. 2010, ApJ, 710, L111
Slysh, V. I., Bachiller, R., Berulis, I. I., et al. 1994, AZh, 71, 37
Sugizaki, M., Mitsuda, K., Kaneda, H., et al. 2001, ApJS, 134, 77
Tsuboi, M., Miyazaki, A., & Okumura, S. K. 2009, PASJ, 61, 29
Ulich, B. L., & Haas, R. W. 1976, ApJS, 30, 247
Val'tts, I. E., Ellingsen, S. P., Slysh, V. I., et al. 2000, MNRAS, 317, 315
Vink, J. 2012, A&A Rev., 20, 49
Wallace, B. J., Landecker, T. L., Kalberla, P. M. W., & Taylor, A. R. 1999, ApJS, 124, 181
Wallace, B. J., Landecker, T. L., & Taylor, A. R. 1994, A&A, 286, 565
Yang, W., Xu, Y., Chen, X., et al. 2017, ApJS, 231, 20
Yusef-Zadeh, F., Cotton, W., Viti, S., Wardle, M., & Royster, M. 2013, ApJ, 764, L19
Yusef-Zadeh, F., Goss, W. M., Roberts, D. A., Robinson, B., & Frail, D. A. 1999, ApJ, 527, 172
Yusef-Zadeh, F., Hewitt, J. W., & Cotton, W. 2004, ApJS, 155, 421
Yusef-Zadeh, F., Law, C., & Wardle, M. 2002a, ApJ, 568, L121
Yusef-Zadeh, F., Law, C., Wardle, M., et al. 2002b, ApJ, 570, 665
Yusef-Zadeh, F., Wardle, M., Rho, J., & Sakano, M. 2003, ApJ, 585, 319
Zubrin, S. Y., & Shulga, V. M. 2008, in Young Scientists 15th Proceedings, eds. V. Y. Choliy & G. Ivashchenko, 41